Bidisperse suspension balance model

Amanda A. Howard, Martin R. Maxey, and Stany Gallier

Phys. Rev. Fluids **7**, 124301 — Published 2 December 2022

DOI: 10.1103/PhysRevFluids.7.124301

A bidisperse suspension balance model

Amanda A. Howard,[1] Martin R. Maxey,[2] and Stany Gallier[3,*]

[1] *Pacific Northwest National Laboratory, Richland, WA*
[2] *Division of Applied Mathematics, Brown University, Providence, RI*
[3] *ArianeGroup, Vert-le-Petit, France*

(Dated: November 15, 2022)

The suspension balance model (SBM) for viscous Stokes flow has been well studied for the case of identical, monodisperse spherical particles in a channel, however, more work remains to be done to explore the bidisperse and polydisperse SBM. We present a simple extension of the SBM that allows for modeling of suspensions of particles of bidisperse size. The comparison with available experiments and direct simulations is found to be good. Additionally, we present a range of simulations to justify the assumptions made in the polydisperse suspension balance model for non-Brownian, neutrally buoyant particles that vary in size with a bidisperse distribution. The aim is to study the effects of moderate size variation on the rheology of the suspension and the distribution of the particles across the flow, especially in the near-wall regions. It is shown that, at the size ratios considered, bidispersity in the particle size does not significantly affect rheological parameters including the particle volume fraction and relative viscosity in the bulk of a Couette flow. The particle phase stresses are distributed between small and large particles in proportion to the relative volume fractions of each species. In bidisperse suspensions, the large particles in the wall layer develop a spatial structure and form chains in the streamwise direction.

PACS numbers: 47.15.G-, 47.57.E, 47.55.Kf, 47.60.Dx
Keywords: Stokes flow, Viscous suspensions, Particle dispersion, Bidisperse, Suspension Balance Model

* stany.gallier@ariane.group

I. INTRODUCTION

Flows of suspended particles with disparate sizes are ubiquitous in both natural and industrial applications including materials processing, food and beverage manufacturing, and microfluidic cell sorting [1–4]. Questions are often posed as to whether the particles separate by size and how the rheology of the suspension is affected by variations in the particle size ratio. In the present study, we consider bidisperse suspensions of spherical, non-Brownian particles in a wall-bounded Couette flow.

Experiments have shown that even in the zero Reynolds number Stokes flow limit, where the flow is linear and reversible, the presence of particles induces chaos and irreversibility at sufficient volume fraction, ϕ, and accumulated strain, $\dot{\gamma}t$, where $\dot{\gamma}$ is the strain rate [5–8]. In this work, we focus on neutrally buoyant non-Brownian particles with large Peclet number. In the case of two spherical particles in a shear flow, small irregularities of the particle surface or shape prevent contact of the particles as they interact due to the flow [9–11]. Subsequent studies by Da Cunha and Hinch [12] calculated the change between initial and final streamlines for two rough particles flowing past each other in a shear flow, showing that rougher particles have a larger net displacement. Zarraga and Leighton Jr. [13] extended this work to bidisperse particle sizes. When a small and large particle with a small, finite surface roughness come into near-contact in a shear flow both particles undergo a net, irreversible displacement, with the smaller particle having a larger net displacement. Further work by Meunier and Bossis [14] indicates that the self-diffusion of particles in a shear flow decreases sharply in bidisperse suspensions.

Early experiments with a densely packed suspension of bidispersed particle with size ratio $\lambda = 0.255$ and total volume fraction $\phi_T = 0.6$ were completed by Graham *et al.* [15] in a wide-gap annular Couette flow device at low Reynolds number. The particles migrated to the lower shear rate region at the outside wall of the device and while the large and small particles could not be imaged separately, the particle layering at the outside wall suggests that the wall layer consisted only of large particles. Similar size segregation in bidisperse suspensions has been seen in various configurations where the shear rate varies across the channel because large particles have been shown to migrate to regions of lower shear faster than small particles [16]. In Poiseuille flow, this faster large particle migration results in enrichment of large particles at the channel centerline where the shear rate goes to zero [17–22].

The earliest simulations of bidisperse suspensions in a shear flow were completed with Stokesian Dynamics for a monolayer of particles confined to a plane of shear, see Chang and Powell [23, 24, 25, 26]. These simulations found that the average cluster size in a bidisperse suspension decreases due to the presence of small particles, resulting in a lower effective shear viscosity [23]. Stokesian Dynamics has been used more recently for fully three-dimensional simulations of bidisperse suspensions of colloidal particles in a uniform shear flow in a periodic domain using Spectral Ewald Accelerated Stokesian Dynamics [27] to study the short-time transport and diffusion properties of a system of bidisperse colloidal particles [28, 29]. Recently, Pednekar *et al.* [30] used discrete element modeling with the lubrication flow description of hydrodynamic interactions to quantify the relative viscosity and normal stress differences for densely packed bidisperse and polydisperse suspensions of frictional particles, with size ratios $\lambda = 0.25 - 0.5$. These numerical simulations have all considered periodic representations of unbounded domains. Chun *et al.* [21] used lattice Boltzmann simulations with walls consisting of fixed particles. These "bumpy" walls may obscure wall layering that was seen in Graham *et al.* [15], Hampton *et al.* [31], Snook *et al.* [32].

Previous simulations are at the particle-scale and—although they are instrumental in understanding physics—they are too computationally involved to handle migration and segregation in complex industrial flows. This generally calls for a continuum version where fluid and particles are lumped together into a homogenized system. Many models are reported in the literature (*e.g.*, see Vollebregt *et al.* [33] for a detailed list) but they fall into the two following classes: diffusive flux models or suspension balance models. Diffusive flux models follow the ideas of Leighton and Acrivos [34] and consider a phenomenological description of migration based on different empirically-fitted diffusive-like terms, like the well-known Philipps model [35]. Work by Chun *et al.* [21] requires hand fitting four parameters to simulation results. On the other hand, the suspension balance model (SBM) attempts to relate the migration flux and the suspension rheology based on volume-averaged balances of mass and momentum for the fluid and particle phases. Relying on the ideas of Nott and Brady [36], Morris and Boulay [37] developed a simple, and now widely used, model in which the migration flux is found to be directly proportional to the gradient in the particle stress. Diffusive flux models are phenomenological models that are generally satisfactory for most flows but can fail in certain situations, such as curvilinear flows. Suspension balance models have stronger theoretical grounds and are therefore expected to be more general.

However, most work looks at suspensions of monodisperse particles and less is known for suspensions having different size classes or significant size distribution. Available works in the literature have mostly relied on an extension of the diffusive flux model to binary suspensions [20, 21, 38, 39]. As far as we are aware, SBM applied to binary mixtures are extremely scarce. Vollebregt *et al.* [33] have considered such models together with highly complex closures for the particle stress [40, 41]. This model suffers from a lack of validation and our experience is that it sometimes leads to spurious results. Norman *et al.* [42] addressed pressure-driven flows with bimodal negatively buoyant particles.

They proposed an extension of the SBM assuming that the particle pressure of each particle species i shares with the relative volume fraction ϕ_i/ϕ. They obtained a relatively fair agreement with their experiments. Lyon and Leal [17] considered a SBM assuming the binary suspension behaves as a monodisperse system consisting of the large particles with liquid and small particles lumped together into an effective suspending fluid. Agreement with their experiments was poor, suggesting that the presence of small particles influences the overall flow and cannot be reduced to an increase in viscosity of the background fluid.

From this literature survey, we conclude that work in developing SBM for bidisperse suspensions is still limited. The purpose of this work is to propose a SBM for bidisperse suspensions. It takes its roots from the Morris-Boulay model [37] and has extended to two classes of particles with different sizes. However, doing so leads to new and unknown quantities (*e.g.*, how the stress is shared between species) which require specific constitutive relations to close the system. Therefore, in this work, we follow a multiscale approach by first using fully-resolved particle simulations to gain insight into the rheology of bidisperse suspensions and then subsequently derive a constitutive model to close our suspension balance model. Since direct numerical simulations of bidisperse suspensions are very scarce in the literature, an originality of this work is to rest on two different numerical methods (Force Coupling Method and Fictitious Domain), which we believe strongly strengthens the confidence in the obtained results.

II. SUSPENSION BALANCE MODEL

A. Monodisperse model

The model proposed in our work is strongly related to the well-known Suspension Balance Model (SBM) proposed by Morris and Boulay [37] and we first start by providing an overview of this model. The suspension is homogenized as an equivalent incompressible fluid. Under Stokes flow assumptions, the suspension is governed by

$$\nabla \cdot \mathbf{u} = 0 \tag{1}$$

$$\nabla \cdot \mathbf{\Sigma} = 0 \tag{2}$$

where $\mathbf{u}$ is the average suspension velocity vector and $\mathbf{\Sigma}$ the suspension stress. The suspension stress is given as the sum of the suspending fluid stress $2\eta_f\mathbf{E}$ and the particle stress modeled as

$$\mathbf{\Sigma}^p = 2(\eta_s - \eta_f)\mathbf{E} - \eta_n\dot{\gamma}\mathbf{Q} \qquad \mathbf{Q} = \begin{bmatrix} 1 & 0 & 0 \\ 0 & \lambda_2 & 0 \\ 0 & 0 & \lambda_3 \end{bmatrix} \tag{3}$$

where $\mathbf{E}$ is the local bulk suspension rate of strain, η_s is the suspension shear viscosity, η_f is the viscosity of the fluid, and η_n the normal stress viscosity both depending on the volume fraction ϕ. Anisotropy parameters are taken to λ_2=0.8 and λ_3=0.5 [37]. An isotropic assumption $\mathbf{Q}$=$\mathbf{I}$ is also a common choice, which will be made here.

The evolution equation for volume fraction ϕ reads

$$\frac{\partial \phi}{\partial t} + \mathbf{u} \cdot \nabla\phi = -\nabla \cdot \mathbf{j} \tag{4}$$

with the migration flux $\mathbf{j}$ given by

$$\mathbf{j} = \frac{2a^2}{9\eta_f} f(\phi) \nabla \cdot \mathbf{\Sigma}^p \tag{5}$$

where a is the particle radius and $f(\phi)$ is the hindrance function classically given by a Richardson-Zaki form of the kind $f(\phi)$=$(1-\phi)^\alpha$ with α=$4 \sim 5$. There are closures available for shear and normal viscosities as

$$\eta_s(\phi) = \left(1 - \frac{\phi}{\phi^c}\right)^{-2} \tag{6}$$

$$\eta_n(\phi) = 1.33 \left(\frac{\phi}{\phi^c}\right)^3 \left(1 - \frac{\phi}{\phi^c}\right)^{-2} \tag{7}$$

where ϕ^c is the critical volume fraction. This is taken to be ϕ^c=0.68 in the initial Morris-Boulay paper [37] but more recent experiments for monodisperse suspensions indicate $\phi^c \approx 0.59$ is a more relevant value for non-Brownian suspensions [43, 44].

B. Bidisperse suspension balance model

In this paper, we propose a SBM for bidisperse suspensions. We start from the same ideas as developed by Morris and Boulay [37] but extended to two classes of particles with different sizes, which was the idea already proposed by Norman *et al.* [42]. The model shares the same sound theoretical grounds as the initial Morris-Boulay model but new quantities arise that are not reported experimentally. A novelty of the present work is to propose closures for those new quantities that will be taken from particle-resolved simulations.

In the following, we consider a suspension composed of two classes of particles i, $i = 1, 2$. The total volume fraction is ϕ=ϕ_1+ϕ_2. The bidisperse suspension flow is still given by Eq. (1) and Eq. (2). To extend the SBM to multiple particle sizes in the same simulation, we write the monodisperse SBM for each phase i

$$\frac{\partial \phi_i}{\partial t} + \mathbf{u} \cdot \nabla \phi_i = -\nabla \cdot \mathbf{J}_i \tag{8}$$

for a volume fraction of species i denoted by ϕ_i, time t, and suspension velocity field $\mathbf{u}$. The flux $\mathbf{j}_i$ is given by

$$\mathbf{j}_i = \frac{2a_i^2}{9\eta_f} f_i \nabla \cdot \mathbf{\Sigma}_i^p \tag{9}$$

where a_i is the particle radius and f_i is the hindrance function. The particle stresses are given in the isotropic case by

$$\mathbf{\Sigma}_i^p = 2(\eta_s^i - \eta_f)\mathbf{E} - \eta_n^i \dot{\gamma} \mathbf{I}. \tag{10}$$

The problem now becomes to find the closures for phase-specific hindrance function f_i, normal viscosity η_n^i, and shear stress η_s^i.

For the hindrance functions, experimental correlations are available such a simple correlation by Shauly *et al.* [45]

$$f_i = (1 - \phi_i)/(\eta_s/\eta_f) \tag{11}$$

or the more complex Davis-Gecol correlation [46]

$$f_i = (1 - \phi_i)^{-S_{ii}} \left(1 + \sum_{i \neq j} (S_{ij} - S_{ii}) \phi_j \right) \tag{12}$$

where the S_{ij} are given function of particle size ratio. In our model, Eq. (11) was chosen for simplicity and robustness. Indeed, the Davis-Gecol expression can sometimes lead to unphysical values.

Empirical correlations for shear and normal viscosities as given by Eq. (6) and Eq. (7) are devised for monodisperse suspensions only. However, many experimental works [24, 47, 48] suggest they can still be valid provided that the critical volume fraction ϕ^c is adjusted. The critical volume fraction ϕ_{bi}^c in bidisperse suspensions varies depending on the relative volume fractions and sizes of the small and large particles and the following expression can be found [38, 49]:

$$\phi_{bi}^c = \phi_{mono}^c \left(1 + c \left| \frac{a_1 - a_2}{a_1 + a_2} \right|^{3/2} \left(\frac{\phi_1}{\phi} \right)^{3/2} \left(\frac{\phi_2}{\phi} \right) \right) \tag{13}$$

with $c \approx 1.5$ and with $a_1 > a_2$. The monodisperse critical volume fraction ϕ_{mono}^c is taken to 0.59. Hence, viscosity expressions given by Eq. (6) and Eq. (7) are used while choosing ϕ_{bi}^c as the critical volume fraction. This will be checked in the forthcoming simulations.

Finally, we assume that the phase normal viscosities η_n^i vary between the two cases according to the relative volume fraction:

$$\eta_n^i = (\phi_i/\phi)\eta_n \tag{14}$$

This assumption, already put forward by Norman *et al.* [42], will be justified in the following sections based on numerical results. Shear viscosity may follow this rule too but the quantity η_s^i is not required for modeling segregation in 1D flows and has therefore not been addressed in the scope of this work.

Equations (8)-(14) are solved for unidirectional flow with variations in the direction of the velocity gradient using a finite-difference technique. It is well known that at the centerline of a Poiseuille flow such homogenized models lead to

a singularity: the shear stress $\eta_s\dot{\gamma}$ is constant across the suspension but at the centerline we have $\dot{\gamma}$=0 by symmetry, which implies $\eta_s \to \infty$. To alleviate associated numerical instabilities, we classically add a non-local shear rate $\dot{\gamma}_{nl}$ to the computed flow shear rate $\dot{\gamma}$. This non-local shear rate is defined as [36, 50]

$$\dot{\gamma}_{nl} = \langle a \rangle \frac{u_{max}}{h^2} \tag{15}$$

where $\langle a \rangle$ is the average particle radius, u_{max} the maximum flow velocity, and L_z the channel width. Since it is non-zero at the centerline, it avoids any divergence. This correction is not activated for a Couette flow where there is a non-zero shear rate across the flow.

III. NUMERICAL METHODS

A. The Force Coupling Method

The first set of numerical simulations is completed using the force coupling method (FCM) for spherical particles confined to a planar channel [51]. Previous work on bidisperse suspensions with the FCM has been limited to moderate volume fractions $\phi_T \leq 0.2$ in a periodic domain [52]. An important feature at higher volume fractions is the accurate representation of short-range viscous lubrication forces. A detailed discussion of the FCM procedure for monodisperse particles is given in Yeo and Maxey [51] and Yeo and Maxey [53]. Here, we will present the extension of the lubrication correction, developed for monodisperse particles by Dance and Maxey [54] and Yeo and Maxey [51], to apply to bidisperse particle sizes.

The equation of fluid motion for Stokes flow with FCM is:

$$\nabla p = \mathbf{f} + \mu \nabla^2 \mathbf{u} + \sum_{n=1}^{N_P} \{ \mathbf{F}^n \Delta_M(\mathbf{r}^n) + (G^n \cdot \nabla) \Delta_D(\mathbf{r}^n) \} \tag{16}$$

where p is the pressure, $\mathbf{f}$ represents any external body forces, μ is the fluid viscosity, $\mathbf{u}$ is the fluid velocity, $\mathbf{F}^n$ is the force monopole moment on the nth particle, $\Delta_M(\mathbf{x})$ is the FCM force monopole density distribution or envelope, G^n is the force dipole moment, $\Delta_D(\mathbf{x})$ is the force dipole, and $\mathbf{r}^n$ is a vector representing the relative distance from the center of particle n, $\mathbf{r}^n = \mathbf{x} - \mathbf{Y}^n$.

The monopole and dipole force envelopes, Δ_M and Δ_D, are given by Gaussians scaled by the particle radius a:

$$\Delta_M = \frac{1}{(2\pi\sigma_M^2)^{3/2}} \exp\left(-\frac{\mathbf{x}^2}{2\sigma_M^2}\right) \tag{17}$$

$$\Delta_D = \frac{1}{(2\pi\sigma_D^2)^{3/2}} \exp\left(-\frac{\mathbf{x}^2}{2\sigma_D^2}\right) \tag{18}$$

with $\sigma_M = \frac{a}{\sqrt{\pi}}$ and $\sigma_D = \frac{a}{(6\sqrt{\pi})^{1/3}}$ [55, 56]. A weighted integral of the flow $\mathbf{u}$ determines the particle velocity. Similarly, the FCM stresslet is set so that the weighted integral of the strain-rate is zero for each particle.

Yeo and Maxey [51, 53] demonstrated that FCM with the lubrication interactions is equivalent to solving a mobility problem:

$$\begin{bmatrix} \mathbf{M}_{\mathscr{F}\mathscr{V}} \mathscr{F}^{tot} \\ \mathbf{M}_{\mathscr{F}\mathbf{E}} \mathscr{F}^{tot} + \mathbf{E}^{\infty} \end{bmatrix} = \begin{bmatrix} \mathscr{R}^{-1} + \mathbf{M}_{\mathscr{F}\mathscr{V}} & -\mathbf{M}_{\mathbf{S}\mathscr{V}} \\ \mathbf{M}_{\mathscr{F}\mathbf{E}} & -\mathbf{M}_{\mathbf{SE}} \end{bmatrix} \begin{bmatrix} \mathscr{F}^{lub} \\ \mathbf{S}^{tot} \end{bmatrix} \tag{19}$$

$\mathscr{V}$ is a vector containing the particle translational and angular velocities, $\mathscr{V} = [\mathbf{V}^T, \Omega^T]^T$, with size $(6N_P)$, and $\mathscr{F}$ is a vector containing the monopole particle forces and torques, $\mathscr{F} = [\mathbf{F}^T, \mathbf{T}^T]^T$, also with size $(6N_P)$. $\mathbf{E}^{\infty}$ is the strain rate of the imposed fluid velocity field, and $\mathscr{V}^{\infty}$ corresponds to the translational and angular velocities arising from the imposed external fluid flow field. $\mathbf{S}$ denotes a $(5N_P)$ vector containing the five independent stresslet components for each particle: $\mathbf{S}_{11}, \mathbf{S}_{12}, \mathbf{S}_{13}, \mathbf{S}_{22}, \mathbf{S}_{23}$. Each submatrix $\mathbf{M}_{AB}$ is a mobility matrix which calculates the value of a quantity B given A. Similarly, a matrix $\mathscr{R}_{AB}$ is the resistance matrix that relates A to B. The force and torque vector, $\mathscr{F}^{tot}$, and FCM stresslet vector, $\mathbf{S}^{tot}$, are given by

$$\mathscr{F}^{tot} = \mathscr{F} + \mathscr{R}_{\mathbf{E}\mathscr{F}} \mathbf{E}^{\infty} \tag{20}$$

$$\mathbf{S}^{tot} = \mathbf{S} + \mathscr{R}_{\mathbf{ES}} \mathbf{E}^{\infty} - \mathscr{R}_{\mathscr{V}\mathbf{S}} (\mathscr{V} - \mathscr{V}^{\infty}). \tag{21}$$

The lubrication correction matrix $\mathscr{R}$ is constructed through the pairwise addition of the two particle lubrication resistance matrices as in Stokesian Dynamics [57] and lattice-Boltzmann simulations [58]. The two particle lubrication correction matrices are given by $\mathscr{R}_{2B} = \mathscr{R}_{2B}^{exact} - \mathscr{R}_{2B}^{FCM}$, where $\mathscr{R}_{2B}^{exact}$ denotes the analytical form of the two-body resistance matrix and $\mathscr{R}_{2B}^{FCM}$ is the FCM two-body resistance matrix. The FCM resistance matrix $\mathscr{R}_{2B}^{FCM}$ is found by constructing the two-body FCM mobility matrix for two particles with size ratio λ with varying separation distances, then inverting the matrix to form the FCM resistance matrix. The polynomial fit tool in MATLAB (2017a) is used to fit a fifth degree polynomial for each of the resistance functions [59]. The exact two-body resistance matrices, $\mathscr{R}_{2B}^{exact}$, are taken from Jeffrey and Onishi [60] and Jeffrey [61], and are also available in corrected form in [54, 59, 62–65].

In the simulations it is necessary to choose a cut-off distance for the lubrication forces, which represents the separation at which two particles in the simulation are considered to no longer be coupled by lubrication forces. In practice, the cut-off distance is chosen at the point that $\mathscr{R}_{2B}^{FCM} \approx \mathscr{R}_{2B}$ so the difference between the two terms and thus the lubrication force goes to zero. Bidisperse suspensions add additional complications in calculating the lubrication cut-off distance. If the cut-off distance for a pair of the largest size particles is greater than the diameter of the smallest particle it is possible for a small particle to enter the gap between two large particles. As the resistance functions assume only empty fluid between two lubrication neighbors the analytical functions will no longer be valid. To avoid this, the lubrication cut-off distance must be less than the diameter of the smallest particle in the simulation, which limits the size ratios λ that the method can handle. For very small values of λ, this can result in $\mathcal{R}_{2B}^{FCM} \neq \mathcal{R}_{2B}$ at the cut-off distance, so the lubrication force term will have a jump discontinuity. For size ratios considered in this paper this is not a concern, and consideration of smaller values of λ is left for a future study.

Beyond the hydrodynamics, a short-range particle-particle contact force between the particles is included to model a small particle surface roughness or asperities that prevent particles from overlapping during the simulation or full direct contact between particles. As in previous studies, the contact force between particles α and β, with centers $\mathbf{r}^\alpha$ and $\mathbf{r}^\beta$, acts along the line of centers of the particles and is given by

$$\mathbf{F}_P^{\alpha\beta} = \begin{cases} -6\pi\bar{a}^2\dot{\gamma}F_{ref}\left(\dfrac{R_{ref}^2 - |\mathbf{r}|^2}{R_{ref}^2 - 4\bar{a}^2}\right)^6 \dfrac{\mathbf{r}}{|\mathbf{r}|} & \text{if} \quad |\mathbf{r}| < R_{ref}, \\ 0 \quad \text{otherwise} \end{cases} \tag{22}$$

in which $\mathbf{r} = \mathbf{r}^\beta - \mathbf{r}^\alpha$, R_{ref} is the cut-off distance, and $\bar{a}$ is the reduced radius,

$$\bar{a} = \frac{a_\alpha + a_\beta}{2}. \tag{23}$$

F_{ref} is a constant chosen to so that the minimum gap between two particles of equal radius a is $0.005a$ when $R_{ref} = 2.01a$ [51]. An analogous particle-wall contact force is included to represent the dynamics of the particle interactions with the wall,

$$\mathbf{F}_W^{\alpha} = \begin{cases} -6\pi a_\alpha^2\dot{\gamma}F_{ref,wall}\left(\dfrac{R_{ref,wall}^2 - |Y_\alpha|^2}{R_{ref,wall}^2 - a_\alpha^2}\right)^6 \dfrac{\hat{y}}{|Y_\alpha|} & \text{if} \quad |Y_\alpha| < R_{ref,wall}, \\ 0 \quad \text{otherwise} \end{cases} \tag{24}$$

Here, $|Y_\alpha|$ is the distance between the wall and the y-coordinate of the center of particle α, $\hat{y}$ is the unit vector in the y-direction, normal to the wall, and $R_{ref,wall}$ and $F_{ref,wall}$ are parameters. For the simulations considered here, $R_{ref,wall} = 1.01a$ and $F_{ref,wall} = 100.0$.

The contribution to the particle stress due to the elastic contact forces is found by the dipole moment of the force distribution,

$$\langle\sigma^C\rangle = \frac{N_P}{V}\langle S^C\rangle = \frac{1}{N_P}\sum_{\alpha=1}^{N_P}\sum_{\beta=1}^{N_c(\alpha)}\left[-\frac{1}{2}(\mathbf{r}^\beta - \mathbf{r}^\alpha)\mathbf{F}_P^{\alpha\beta}\right] \tag{25}$$

where $N_c(\alpha)$ is the number of particles within the contact force cut-off of particle α and V is the volume of the domain [66]. The particle contribution to the bulk stress is then the sum of the contribution from the contact stress, S^C, and other stresslet moments from the resolved FCM dipole terms or the lubrication corrections, $S_,$:

$$\langle\sigma_{ij}\rangle = \frac{N_P}{V}\langle S_{ij}\rangle + \frac{N_P}{V}\langle S_{ij}^C\rangle. \tag{26}$$

The particle contact pressure is defined as the trace of the contact stress tensor,

$$\Pi = -\frac{1}{3}(\sigma_{11}^C + \sigma_{22}^C + \sigma_{33}^C). \tag{27}$$

B. Fictitious Domain Method

The second method used in the frame of this study is the fictitious domain (FD) method [67–69] in which solid particles are supposed to be filled with a fluid having the same properties as the actual fluid. Particles are thus considered as some regions of the fluid constrained to have a rigid body motion through an additional momentum forcing $\boldsymbol{\lambda}$. Just like the FCM, the Stokes equations are solved for an incompressible fluid as

$$\nabla \cdot \mathbf{u} = 0 \tag{28}$$

$$-\nabla p + \mu \nabla^2 \mathbf{u} + \rho \boldsymbol{\lambda} = 0 \tag{29}$$

Momentum forcing enforces a rigid body motion inside the particle region. The Stokes equations are solved by finite differencing on a staggered Cartesian grid using standard projection methods. Most numerical details are skipped here for brevity and may be found in Gallier *et al.* [69].

A correction procedure for force, torque, and stresslet is considered for lubrication interactions similarly to Stokesian Dynamics [57, 70] or FCM, as described in the previous section. A grand resistance lubrication matrix $\mathscr{R}$ is constructed by pairwise addition of two-particle lubrication resistance matrices. This two-particle lubrication correction matrix is similarly estimated as $\mathscr{R}_{2B} = \mathscr{R}_{2B}^{exact} - \mathscr{R}_{2B}^{resolved}$, where $\mathscr{R}_{2B}^{exact}$ is the analytical two-body resistance matrix [62] and $\mathscr{R}_{2B}^{resolved}$ is the two-body resistance matrix explicitly resolved by the FD scheme. It is obtained by *a priori* computations for many pairs of particles with different orientation, separation, and size ratio λ and is then tabulated for current configurations during computations. Exact theoretical lubrication functions are taken from the references already cited in the previous section dedicated to FCM. Lubrication correction is only needed for very close particles and is activated whenever the separation distance between particles is smaller than one grid spacing Δ, here taken to be $\Delta = \bar{a}/5$ where $\bar{a}$ is the average particle radius for the considered pair. Since theoretical lubrication functions diverge at contact, this can lead to numerical difficulties when particles come to near-contact. This is alleviated by adding a small value $10^{-6}\bar{a}$ to the actual particle separation when evaluating lubrication functions.

A short-range force is used to model direct contact between particles and avoid particle overlapping. Assuming a soft-sphere Hertzian contact for pair α and β, the normal force $\mathbf{F}_P^{\alpha\beta}$ then reads

$$\mathbf{F}_P^{\alpha\beta} = -k_n \left| \|\mathbf{r}\| - a_\alpha - a_\beta - h_r \right|^{3/2} \frac{\mathbf{r}}{|\mathbf{r}|} \tag{30}$$

Particle roughness is accounted for in the model assuming sparse asperities of size h_r. Contact is therefore supposed to take place whenever $\|\mathbf{r}\| \leqslant a_\alpha + a_\beta + h_r$. Note that lubrication forces are however still evaluated based on the actual separation distance $\|\mathbf{r}\| - a_\alpha - a_\beta$ since the fluid is assumed to flow freely between asperities. In this work, the roughness size is fixed to $h_r/\bar{a} = 5.10^{-3}$, which is a typical roughness measured for suspension particle. The normal stiffness k_n is chosen sufficiently high so as to mimic rigid particles and the non-dimensional stiffness $k_n/\mu\dot{\gamma}\bar{a}^2 h_r^{-3/2}$ is typically 10^5. We check *a posteriori* that the maximum roughness deformation never exceeds one (i.e., none of the asperities are completely deformed). Contacts with the wall are treated in the same way. Rheological quantities and particle stress are computed similarly to FCM with the stress having contributions from the explicitly-resolved flow, lubrication corrections, and contacts.

Both FCM and FD methods share some similarities as they both rely on solving directly the Stokes equations. The additional forcing is distinct in essence and expression but in both cases it accounts for the effect of the particles on the flow field. The way lubrication is accounted for is also quite close although some minor variations may exist in the way FCM/resolved interactions are modeled (polynomial fit vs. tabulation). The two major differences lie in the numerical methods (although not detailed further in the context of this paper, this includes numerical methods to solve Stokes equations or linear systems, grid spacing, etc.) and in the contact force modeling. Although the force model is different, driving parameters such as cut-off distance or force scale are basically in the same range. In any case, our goal is not to strive to closely match those two numerical models: getting the same results twice would not bring much for our study. Rather, the idea was to use them as is—without any change—and assess whether they yield a similar rheology for bidisperse suspensions. If so, this mitigates the risk of errors and strengthens the obtained results on binary suspensions—which is desirable as they have been only scarcely addressed so far.

C. Simulation parameters

The particle size ratio is given by $\lambda = a_S/a_L$, where a_S and a_L are the radii of a small and large particle, respectively. The relative small particle bulk volume fraction, $\beta = \phi_S/\phi_T$, is the ratio of the small particle volume fraction ϕ_S and

the total volume fraction ϕ_T. The large particle volume fraction is then given by $\phi_L = (1-\beta)\phi_T$. The large particle size is kept fixed at $a_L = 1$ and the small particle size is varied so that the large particle radius a_L can be used as a scaling parameter.

The bidisperse simulations are completed in a planar channel with channel width $H_y = 40a_L$ and vorticity dimension $L_x = 30a_L$ for a suspension with total volume fraction 0.4. The channel length in the streamwise direction, L_z, is adjusted depending on the particle size ratio so that the total number of particles in the simulation is on the order of $10^3 - 10^4$. The direction of mean vorticity, x, is denoted by the subscript 1, the wall-normal direction, y, is denoted by the subscript 2, with channel walls at $x_2 = 0$ and $40a_L$, and finally the streamwise direction, z, is denoted by the subscript 3. Periodic boundary conditions are applied in the streamwise (z) and spanwise (x) directions, with planar, no-slip walls in the y direction. A simulation with monodisperse particles is also run to provide a comparison. The simulation parameters are given in table I.

	λ	L_z	ϕ_T	β	$\langle a \rangle$	N_P	f_S
L60_1	0.6	30	0.4	0.25	0.757	6558	0.607
L60_3	0.6	30	0.4	0.75	0.627	12797	0.933
L72_3	0.72	40	0.4	0.75	0.751	10357	0.889
L80_1	0.8	60	0.4	0.25	0.921	8515	0.394
L80_2	0.8	60	0.4	0.50	0.868	10216	0.657
L80_3	0.8	60	0.4	0.75	0.829	11791	0.854
Monodisperse	–	60	0.4	–	1.0	6878	–

TABLE I: List of bidisperse simulation parameters. The last column is the fraction of small particles, $f_S = N_S/N_P$, where N_S is the number of small particles, N_L is the number of large particles, and N_P is the total number of particles, provided as a comparison to other works. $\langle a \rangle$ is the average particle radius, $\langle a \rangle = \frac{N_S a_S + N_L a_L}{N_S + N_L}$, and $\beta = \phi_S/\phi_T$ is the ratio of the small particle volume fraction to the total volume fraction.

For each of the Couette flows the mean shear rate is kept fixed at $\dot{\gamma} = 1$. In both FCM and FD models, the contact force coefficient scales with shear rate, so that results are independent of shear rate and the exact value of $\dot{\gamma}$ is irrelevant. Investigating the role of the shear rate (using a constant force barrier in the simulation) has not been done in the frame of this paper and is left for future studies. Each simulation is run for 100 strain units, then results are averaged over 25 equally spaced time intervals over the subsequent 25 strain units. This study focuses on a single value of volume fraction ϕ_T=0.4. This value of 0.4 was chosen since for this range of fraction, both contact and hydrodynamic forces equally prevail [78]. In addition, the only relevant experiments on bidisperse suspensions [18] (and to which our results will be validated) are obtained for ϕ_T=0.4.

D. Validation tests

Exact results for the relative velocities for two particles in a shear flow can be obtained from Batchelor and Green [71] in terms of three non-dimensional functions and the particle separation distance r,

$$\mathbf{V}(r) = -\dot{\gamma} \begin{cases} r_2(B/2 - r_1^2/r^2(A-B)) \\ r_1(B/2 - r_2^2/r^2(A-B)) \\ r_1 r_2 r_3/r^2(A-B) \end{cases} \tag{31}$$

Here, $\mathbf{r} = (r_1, r_2, r_3)$ is the separation between the particles in the stream-wise, velocity gradient, and vorticity directions, respectively. The values of A, B, and C are given by Batchelor and Green [71] for the far-field case of widely separated spheres for all size ratios λ, and in the near-field case for $\lambda = 1$. The near-field values of A and B for $\lambda = 0.5$ can be found in Pesche [72]. The results of the FCM and FD simulations and the near- and far-field values are shown in Figure 1 for $\lambda = 0.5$, where $\xi = r/a_L$. Good agreement is shown between the values, even when the particles are very close together. In particular, FD and FCM simulations show very similar results.

E. Particle stresses for Couette flow

The total volume fraction profile and the volume fraction profiles of the small and large particles for the FCM simulations is shown in Fig. 2, where the phasic average is defined as in Yeo and Maxey [53], Drew [73]. The volume

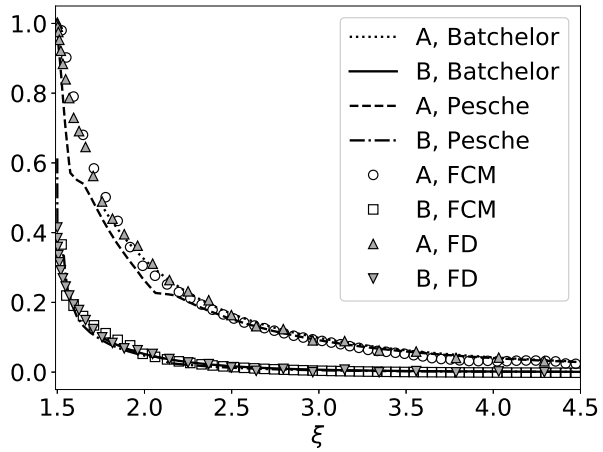

FIG. 1: Values of A and B for two particles in a shear flow for $\lambda = 0.5$ from both FCM and FD. The exact far field solution is given by Batchelor and Green [71] until $\xi = 1.75$. The near field solution is from Pesche [72]. We see excellent agreement between the previous results and the two numerical methods considered here.

fraction profiles in the center of the channel do not change significantly with the bidispersity in the simulations and the volume fraction is constant for $y/a_L > 10$. The first wall layer forms at $y/a_L = \lambda$, with subsequent layers forming adjacent to the wall layer. This layering due to the wall extends out to $y/a_L = 5-6$, and comparing flows with equal volume fractions of large and small particles shows there is a significantly higher volume fraction of small particles than large particles in both the first and second wall layers. The volume fraction of large particles will be higher slightly outside the wall layering to accommodate the large particles that may migrate out of the wall layer during the simulation. This wall layering will be discussed in detail in sec. V.

The normal stress differences are given by

$$\langle N_1 \rangle = \langle \sigma_{33}^P \rangle - \langle \sigma_{22}^P \rangle \tag{32}$$
$$\langle N_2 \rangle = \langle \sigma_{22}^P \rangle - \langle \sigma_{11}^P \rangle \tag{33}$$

where 1,2,3 refers to the the vorticity, velocity gradient, and streamwise directions, respectively. The particle averaged normal stress differences, scaled by the wall shear stress, $\tau = \mu_r \mu \dot{\gamma}$, are shown in Fig. 3. As in simulations for monodisperse suspensions, we find that N_1 and N_2 are negative [57, 74]. Experiments with bidisperse suspensions have again shown that both N_2 and N_1 are negative, and similar in magnitude [27, 75, 76]. Zarraga *et al.* [77] showed that for monodisperse spheres in a shear flow $|N_2| > |N_1|$, and $|N_2| \approx 3.6|N_1|$, while Stokesian Dynamics simulations by Sierou and Brady [57] found that $|N_2| \approx |N_1|$. Here the two normal stress differences are approximately equal in magnitude, with $|N_1| < |N_2|$. Friction is also known to alter N_1 and N_2 [78] but it is not accounted for in the framework of this study. An overall good agreement is noted between FD and FCM simulations. There is a slight disparity—mostly for N_2—which is expected because of the differences in contact force modeling. However both models find that N_1 and N_2 are virtually unaffected by bidispersity for this range of λ.

In Fig. 4 we plot the normal stress difference profiles across the channel, averaged over the channel centerline. Both N_1 and N_2 are negative and approximately uniform in the central portion of the channel away from the wall layer. N_1 becomes positive immediately adjacent to the wall, while N_2 is more negative in the wall layer due to the localized dynamics near the wall. The first normal stress difference N_1 varies slightly with the size ratio, increasing with smaller values of λ. For N_2 there is no significant difference with λ for the size ratios considered.

An understanding of this behavior of the normal stress differences can be found by looking at the particle stress profiles at the channel wall in Fig. 5. σ_{33} becomes less negative at the channel wall, while σ_{22} becomes more negative, resulting in a positive value for N_1. The value of σ_{11} becomes slightly less negative at the channel wall, so N_2 becomes more negative. This behavior was already noted in [79] and is due to wall layers as it will be shown in Sec. V. The formation of chains in the direction of the flow reduces the contact stress in that direction 3, hence a significant reduction in $|\sigma_{33}|$ as noted in Fig. 5. The relative contributions to the stress profiles from the small and large particles are also plotted in Fig. 5.

A major finding of this work is that the particle stresses are divided relative to the volume fraction of each species,

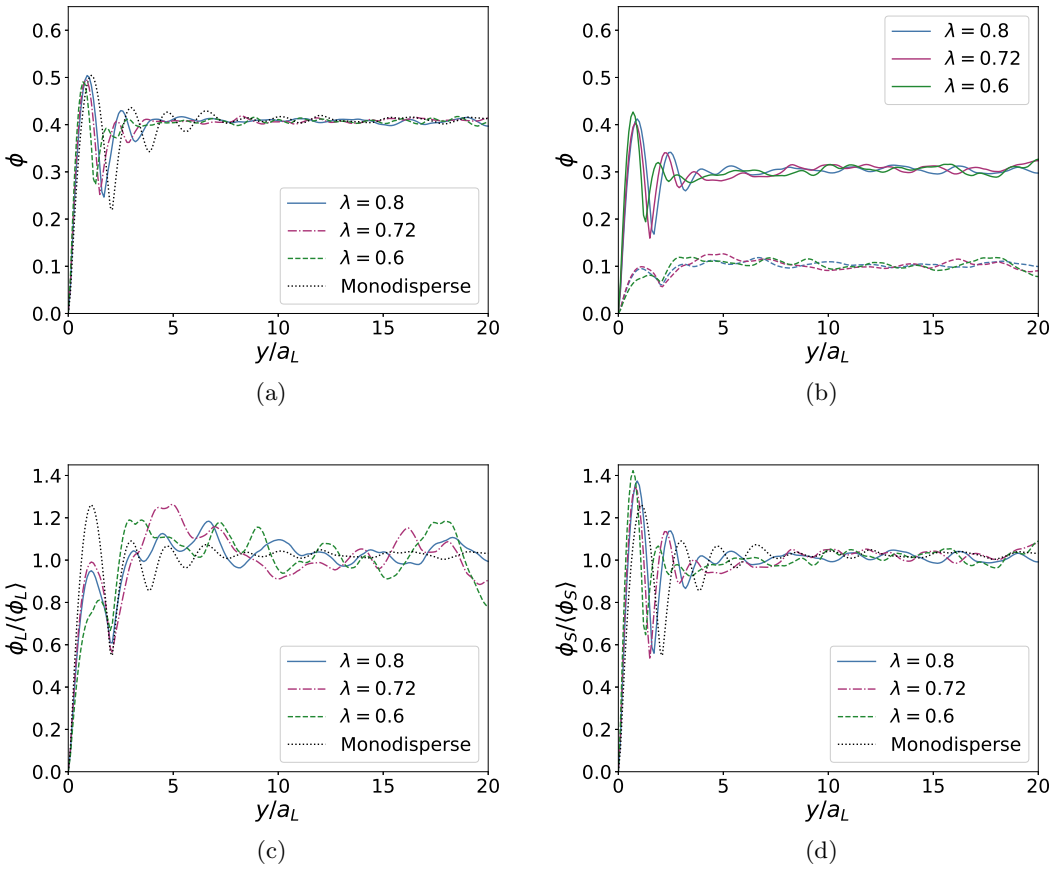

FIG. 2: (a) Total volume fraction profile. (b) Solid lines: small particle volume fraction profile. Dashed lines: large particle volume fraction profile for $\lambda = 0.8, 0.72$, and 0.6 with $\beta = 0.75$, compared to a monodisperse simulation, averaged over $\dot{\gamma}t = 100 - 125$. The channel wall is at $y/a_L = 0$ while the channel centerline is at $y/a_L = 20$ (FCM simulations). (c) Large particle volume fractions scaled by the average large particle volume fraction ($\langle\phi_L\rangle = 0.1$) and monodisperse volume fraction scaled by the average monodisperse volume fraction ($\phi = 0.4$). (d) Small particle volume fractions scaled by the average small particle volume fraction ($\langle\phi_S\rangle = 0.3$) and monodisperse volume fraction scaled by the average monodisperse volume fraction.

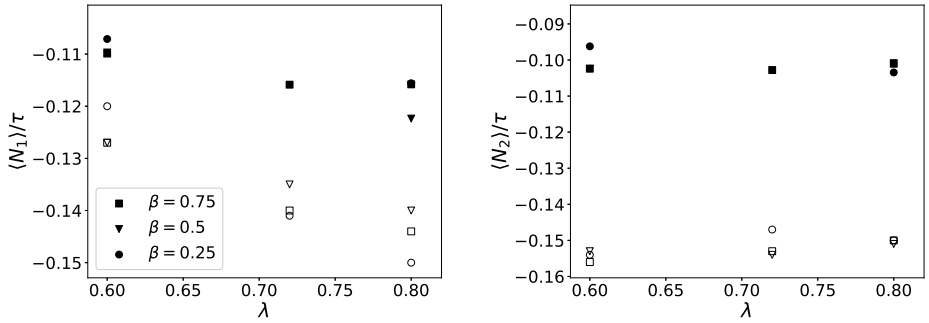

FIG. 3: Average normal stress differences for bidisperse suspensions at a range of particle size ratios and small particle volume fractions averaged over all particles for $\dot{\gamma}t = 100 - 125$. Left: N_1. Right: N_2. Filled symbols: FCM. Empty symbols: FD. Averages are taken over the domain $5a_L \leq y \leq 35a_L$ to exclude the wall layer.

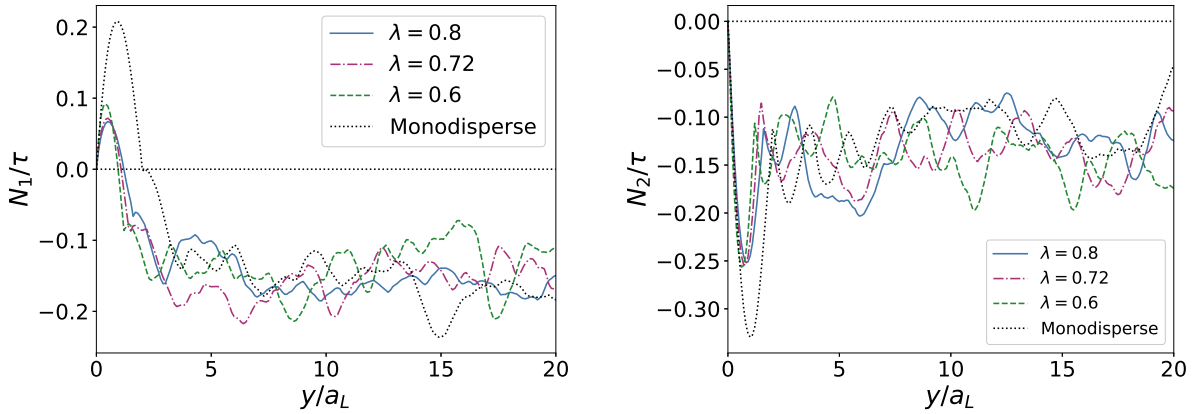

FIG. 4: Normal stress difference profiles N_1 (left) and N_2 (right) from FCM simulations for varying λ at $\beta = 0.75$ and a monodisperse suspension averaged over $\dot{\gamma}t = 100 - 125$. Both N_1 and N_2 are negative on average across the channel, however N_1 is positive in the wall layer.

with

$$\frac{\langle \sigma_{ij}^S \rangle}{\langle \sigma_{ij}^L \rangle} \approx \frac{\phi_S}{\phi_L}.$$

This is demonstrated in Fig. 6, where the relative volume fractions of the small and large particles are compared to the average contributions to the total stress from the small and large particles. The data fits very well to a linear fit, in agreement with the results from Wang and Brady [27] for total volume fraction $\phi = 0.45$. This result is at the core of the present SBM model, accounted for by Eq. (14). It is interesting to pinpoint that this result is found both by FCM and FD simulations, which is believed to strengthen the relevance and generality of this conclusion.

Finally, we can consider the contact pressure profile for bidisperse Couette flows in Fig. 7. Previous work for non-Brownian suspensions in shear flow has shown that particle migration across the channel is closely linked to gradients in the particle contact pressure [80]. Here, the particle volume fraction profiles are constant across the channel with no significant gradients in the contact pressure other than near the wall, where the wall contact force balances the particle-particle contacts. The contact pressure outside the wall layer decreases slightly with smaller values of λ, and at the core of the channel the monodisperse suspension has a larger particle contact pressure than any of the bidisperse simulations.

In all the quantities considered in this section, including the maximum volume fraction, the relative viscosity, the stress profiles, and the volume fraction profiles, the bidisperse suspensions behave in a very similar manner to a monodisperse suspension. Any variation shown, such as in the contact pressure, is relatively small compared to the overall magnitude of the quantity. This is partly because there is not a significant variation in the maximum volume fraction at the particle size ratios considered. In addition, segregation of bidisperse suspension flows has been shown to occur when there is a gradient in the shear rate, as the induced particle velocity in the cross-stream direction then depends on the particle size. In a Couette flow, there is no particle migration flux, and thus no mechanism for size-induced segregation.

IV. BIDISPERSE SUSPENSION BALANCE MODEL RESULTS

In the previous section, we showed that the stresses in a suspension of bidisperse particles in a Couette flow are distributed proportionally to the relative volume fractions of each population of particles. In particular, the total stress (and contact pressure) is the same for monodisperse and bidisperse simulations, at least for the moderate size ratios investigated. In this section, we show how the bidisperse SBM we have proposed compares with FCM simulations of a dense Poiseuille flow and also with experiments.

Fig. 8 and Fig. 9 compare the SBM and FCM simulations of Poiseuille flow with $\lambda = 0.6$ and $\lambda = 0.8$, respectively, and $\beta = 0.25, 0.5$, and 0.75 for $\phi_T = 0.4$. In Fig. 8 the accumulated strain is $\dot{\gamma}t = 320$ and in Fig. 9 the accumulated strain is $\dot{\gamma}t = 265$. The SBM performs well here. Overall, the bidisperse SBM is able to accurately predict the particle volume fractions across the channel outside the wall layer, defined by $y/a_L \leq 5$. This latter point will be addressed

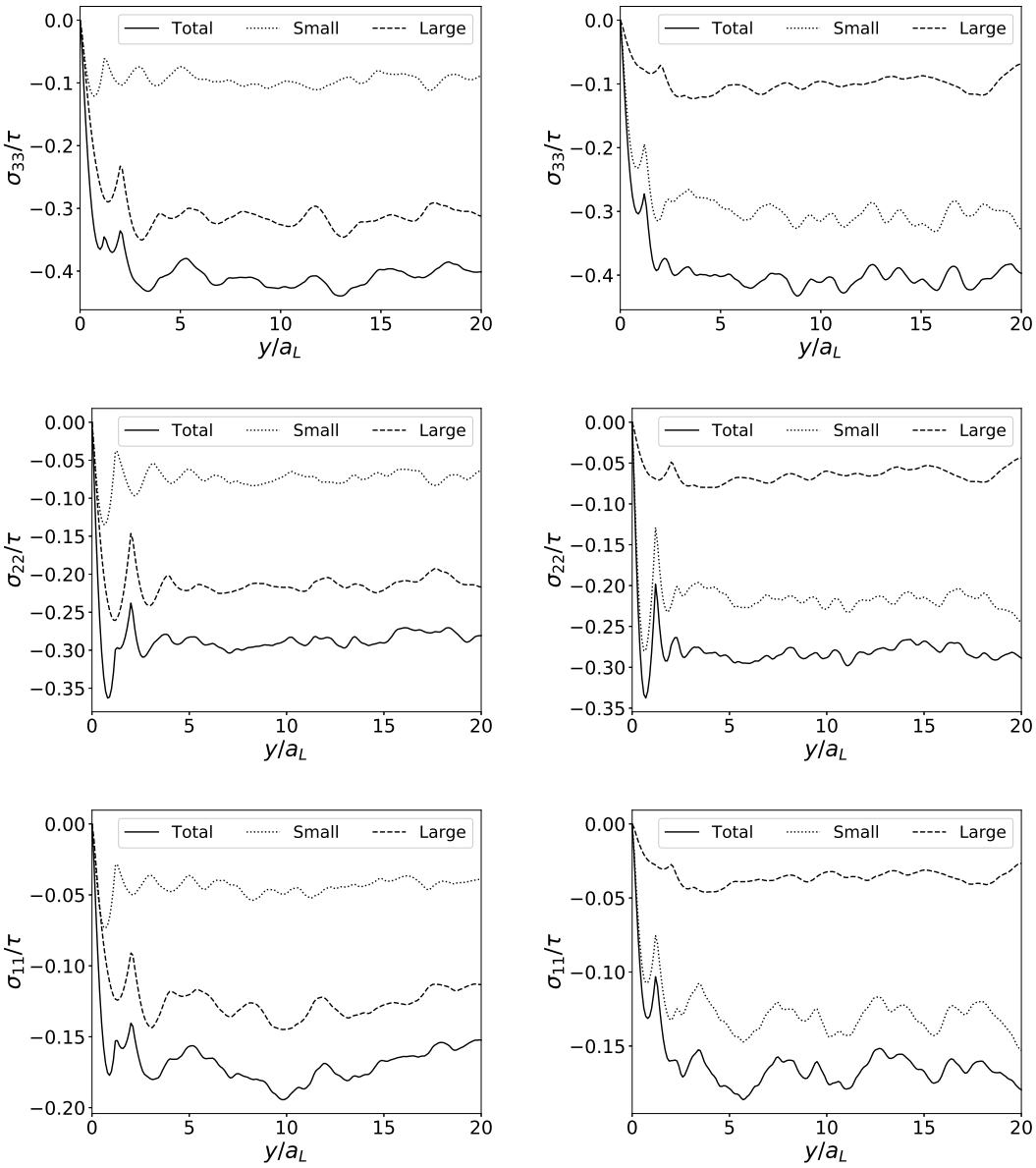

FIG. 5: Stress profiles σ_{33} (top row), σ_{22} (middle row), σ_{11} (bottom row) for $\lambda = 0.6$ for $\beta = 0.25$ (left column) and $\beta = 0.75$ (right column) averaged over $\dot{\gamma}t = 100 - 125$ (FCM simulations). The stress for each size particle is distributed by the relative volume fraction of each species.

in the next section. We note in particular that small particles are likely to migrate when they are present in large quantities ($\beta = 0.75$). This contrasts to the usual assumption that only the largest particles can migrate significantly.

In Fig. 10 we compare the SBM with two experimental cases from Semwogerere and Weeks [18]. The channel width is $H_y = 32a_L$. The particles have a size ratio of $\lambda = 0.5$. In Fig. 10a, $\phi_L = \phi_S = 0.1$, with a total volume fraction of $\phi_T = 0.2$. In Fig. 10b, $\phi_L = 0.25$ and $\phi_S = 0.1$, with a total volume fraction of $\phi_T = 0.35$. The SBM is calculated at a strain $\dot{\gamma}t = 1500$ as in experiments, and the FCM results are at strain $\dot{\gamma}t = 280$ due to computational time limitations. For both cases we compare with the bidisperse SBM results and experimental results. The bidisperse SBM results agree with experiments, although they do not show the segregation dip that occurs at the center of the channel for the large particle volume fraction in [18]. One explanation for this is that the FCM simulations do not consider Brownian motion. In the experiments (where the particle size is about 1 μm), Brownian motion may be responsible for small particles migrating away from the centerline, where they can be replaced by large particles migrating towards the center. In comparison, with FCM or SBM there is no force to remove particles from the centerline.

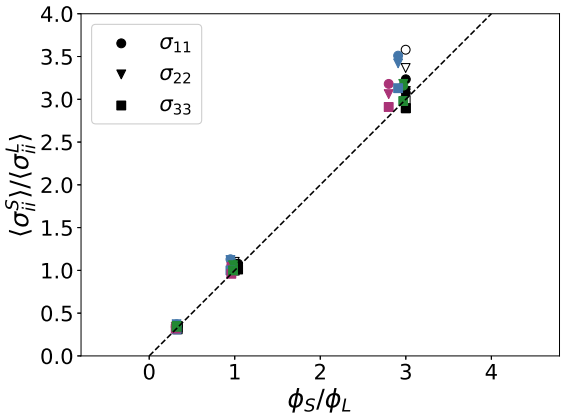

FIG. 6: Ratio of particle stresses for small and large particles compared to a linear fit (dashed line) for FCM with $\lambda = 0.8$ (filled symbols) and $\lambda = 0.6$ (empty symbols) and FD $\lambda = 0.8$ (green), $\lambda = 0.72$ (red), and $\lambda = 0.6$ (blue) averaged over $\dot{\gamma}t = 100 - 125$. The relative contribution to the total stress from the small and large particles is directly proportional to the relative volume fractions of the small and large particles.

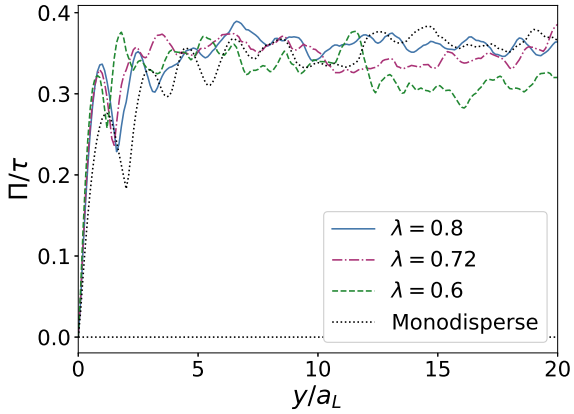

FIG. 7: Profile of the total particle contact pressure, averaged over strain interval $\dot{\gamma}t = 100 - 125$ for $\beta = 0.75$ and a monodisperse suspension (FCM simulations). The pressure is constant across the channel outside of the region adjacent to the wall and increases slightly with λ.

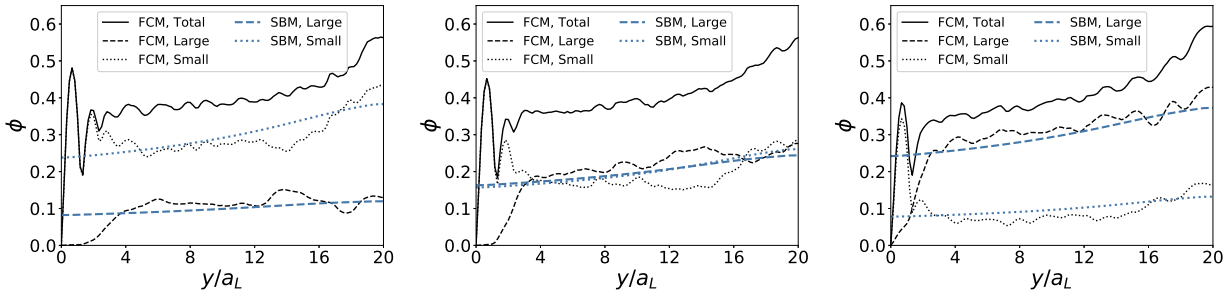

(a) $\beta = 0.75$ (b) $\beta = 0.5$ (c) $\beta = 0.25$

FIG. 8: Volume fraction profiles for $\lambda = 0.6$ and $\beta = 0.75$ (a), 0.5 (b), and 0.25(c). Comparisons between SBM and FCM simulations at strain $\dot{\gamma}t = 320$.

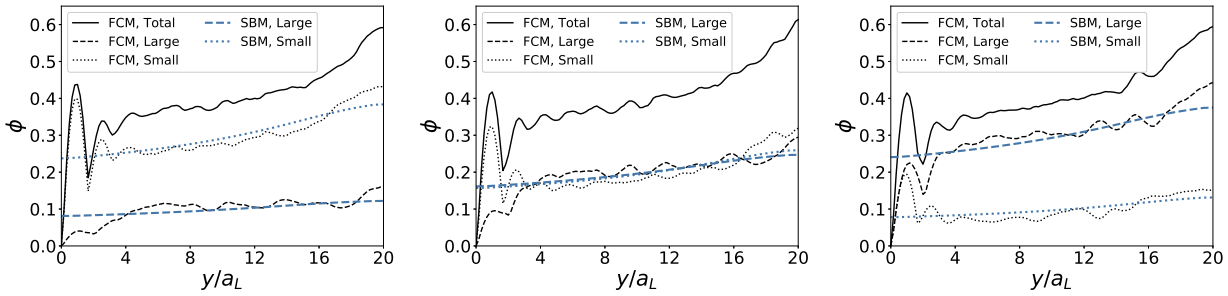

(a) $\beta = 0.75$ (b) $\beta = 0.5$ (c) $\beta = 0.25$

FIG. 9: Volume fraction profiles for $\lambda = 0.8$ and $\beta = 0.75$ (a), 0.5 (b), and 0.25(c). Comparisons between SBM and FCM simulations at strain $\dot{\gamma}t = 265$.

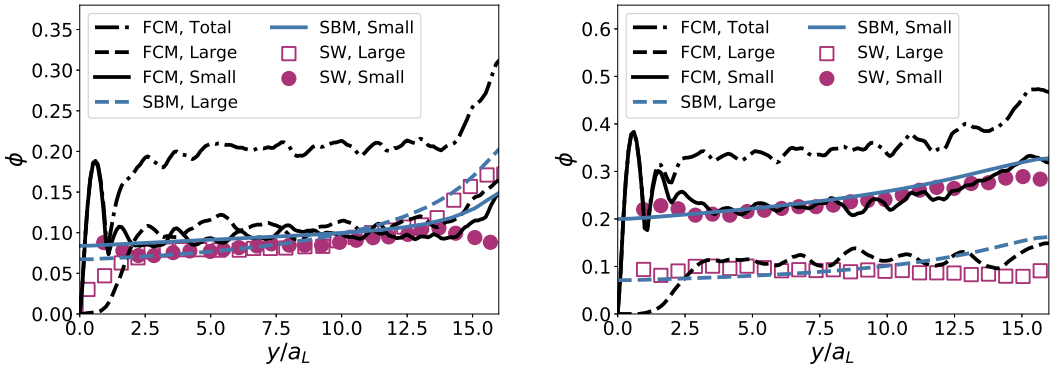

(a) $\phi_T = 0.2$ and $\beta = 0.5$ (b) $\phi_T = 0.35$ and $\beta = 0.29$

FIG. 10: Volume fraction profiles: comparisons between SBM, FCM simulations and experiments (SW)[18] ($\lambda = 0.5$). $\phi_T = 0.2$ and $\beta = 0.5$ (a); $\phi_T = 0.35$ and $\beta = 0.71$ (b). SBM results are computed for a strain $\dot{\gamma}t = 1500$ and FCM results are at strain $\dot{\gamma}t = 280$. The results from [18] are scaled by an additional factor of $\sigma = 1.04$ so that $H/(a_L\sigma) = 32$ to provide a direct comparison with the FCM and SBM results (in [18], $H = 50\,\mu$m, $a_L = 1.5\,\mu$m, and $a_S = 0.69\,\mu$m, so $\lambda = 0.460$.)

V. WALL LAYERING

In Fig. 8, it is apparent that in steady-state for the FCM simulations the volume fraction of large particles in the wall layer drops to zero. This trend is less clear when the size ratio λ is larger in Fig. 9. In fact, the dynamics of the wall layer for both the Couette and Poiseuille flow are fascinating, and we present some details here. The wall layer dynamics are not accounted for in the SBM simulations. This was anticipated because such models result from a homogenization procedure and can therefore not capture length scales below a few particle diameters. However, a thorough understanding of the wall layers can contribute to future refinements of the bidisperse SBM.

As we noted above, the wall layer consists predominately of small particles with $\lambda = 0.6$ in a Poiseuille flow. An understanding of why can be found by studying the wall layers of Couette flows. In Fig. 11, we show a snapshot of the wall layer located one small particle radius above the wall. It is evident that the large particles are clustered together, forming chains in the streamwise direction. A quantitative look at the orientation between pairs of touching particles is seen in Figure 12. Large particles are predominately aligned in the streamwise direction, while small particles are relatively uniformly distributed at a distance $2a_s$ from the particle center, with a slight preference for forming chains in the direction of flow. Looking at small-large and large-small particle interactions, we see that small and large particles are most likely to collide perpendicularly to the direction of fluid flow. To understand this, we consider a collision between a small and large particle. The force between the two particles is in the direction of the vector connecting the centers of these two particles. In the case of a collision between a small and large particle, the force vector has a small component perpendicular to the wall, which pushes the small particle closer to the wall and

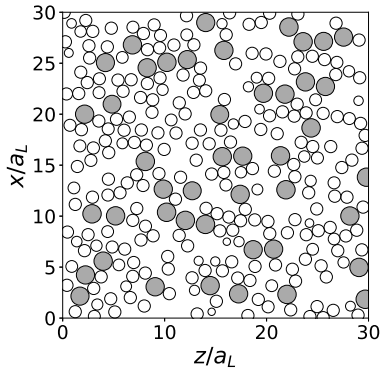

FIG. 11: Example of the wall layer in a Couette flow with $\lambda = 0.6$ and $\beta = 0.5$ intersecting the plane $y = a_s$ at $\dot{\gamma}t = 100$ (FCM simulations). The small particles are shown as empty circles and the large particles are shown as filled circles.

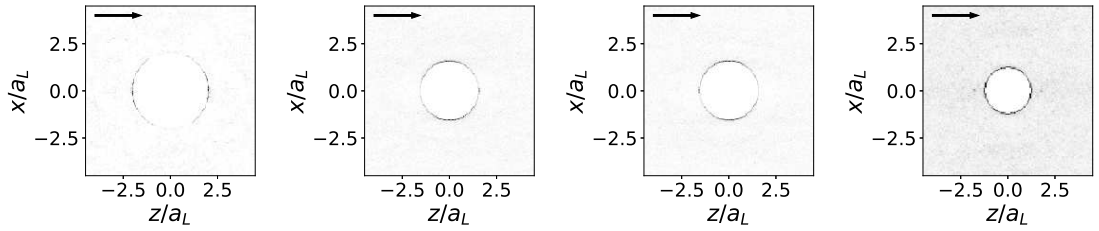

(a) Large-large, $\beta = 0.5$ (b) Large-small, $\beta = 0.5$ (c) Small-large, $\beta = 0.5$ (d) Small-small, $\beta = 0.5$

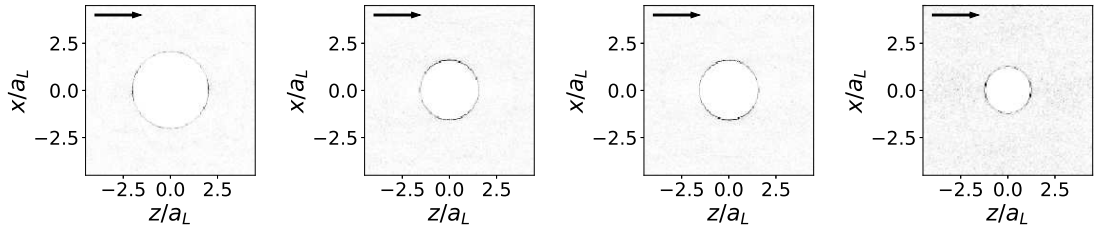

(e) Large-large, $\beta = 0.25$ (f) Large-small, $\beta = 0.25$ (g) Small-large, $\beta = 0.25$ (h) Small-small, $\beta = 0.25$

FIG. 12: Pair-correlation function of the relative distances between particle centers with $\lambda = 0.6$ and $\beta = 0.5$ (a-d) and $\beta = 0.25$ (e-h) for a Couette flow (FCM simulations). We consider the interactions between small and large particles separately. The flow is sampled at the top and bottom walls on the planes $y = a_s$ and $y = H_y - a_s$ at 40 timesteps equally spaced between $\dot{\gamma}t = 25$ and $\dot{\gamma}t = 125$. The arrow indicates the direction of flow.

the large particle away from the wall. Thus, the large particles will, over time, exit the wall layer. In order for a large particle to remain in the wall layer it must predominately have collisions with other large particles and not engage in collisions with small particles, thus the formation of large particle chains in the streamwise direction.

VI. CONCLUSIONS

In this paper we examine the effect of moderate particle size variations on a dense suspension Couette and Poiseuille flows by numerical simulations at particle scale. At the size ratios λ considered (0.6∼0.8), the bidispersity leads to no significant change in rheological parameters of the suspension for the Couette case, including the particle volume fraction and relative viscosity. The results shown here for the normal stress differences and relative viscosity agree well with previous results from numerical simulations of bidisperse suspensions in periodic domains. Also in agreement

with previous studies, the particle stresses are distributed proportionally to the relative volume fractions of small and large particles. This result was confirmed with two different numerical approaches (FCM and FD). The particle contact pressure does show a slight variation with changes in the particle size ratio λ, but at the size ratios considered here the difference is small.

Due to limitations in particle manufacturing, many experiments may use particles with size variations of up to 10%. The results in this paper demonstrate that numerical simulations with monodisperse sizes can accurately capture the rheology of such a suspension. Variations in particle sizes may have a greater effect at lower values of λ than considered here. In particular, with larger size variations the maximum volume fraction of the suspension may increase as the small particles can fill in gaps between the large particles at maximum packing.

This work also proposes a new suspension balance model (SBM) for bidisperse suspensions. It is based on extending the usual SBM for two size classes and using the result that normal stresses share with the relative particle fraction. An overall good agreement is found between this SBM and direct simulations of Poiseuille flows as well as with experiments. In particular, small particles can also migrate to the centerline when they are present in sufficient quantity.

Future work might consider direct simulations for larger size ratios in order to improve and validate the SBM for a wider range of suspensions. Also, the effect of volume fraction needs to be investigated to assess whether SBM is likely to be predictive for the whole range of volume fractions, including very dense suspensions. Stokes flow is inherently linear so varying the shear rate on the face of it should not have an effect. However, in our simulations we have the irreversible effects of the contact barrier. Usually we have set this to give a specific minimum gap width, which means our force coefficient scales with shear rate. If we fixed the barrier force parameters, then varying the shear rate would give different minimum gaps and different shear viscosities or normal stresses. Lubrication forces will have a stronger effect as the minimum gap decreases. You see a bit of this between FCM and FD results given the different parameterizations of the force barrier. Investigating this effect could be part of future studies; the fraction profiles at steady state however do not depend on the shear rate for SBM. The simulations conducted so far showed a depletion of large particles at the wall that is missed by the SBM. A first physical mechanism has been proposed and could be included in the future in an improved SBM to provide more reliable predictions in the near-wall region.

ACKNOWLEDGMENTS

A.A.H. acknowledges support by the National Science Foundation Graduate Research Fellowship under Grant No. DGE 1058262. Additional support by the U.S. Department of Energy Office of Science under Award Number DE-SC0009247 is gratefully acknowledged. This research was conducted using computational resources and services at the Center for Computation and Visualization, Brown University. Pacific Northwest National Laboratory is a multi-program national laboratory operated for the U.S. Department of Energy (DOE) by Battelle Memorial Institute under Contract No. DE-AC05-76RL01830. S.G. acknowledges support by French Procurement Agency (DGA).

[1] J. Kromkamp, F. Faber, K. Schroen, and R. Boom, "Effects of particle size segregation on crossflow microfiltration performance: Control mechanism for concentration polarisation and particle fractionation," J. Memb. Sci. **268**, 189–197 (2006).
[2] S. Bodenstab, M. Juillerat, W. Bauer, and K. Sommer, "Separating the Role of Particles and the Suspending Fluid for the Flow of Soy Milks," J. Food Sci. **68**, 1722–1730 (2003).
[3] T. M. Morris, "The Relationship Between Haze and the Size of Particles in Beer," J. Inst. Brew. **93**, 13–17 (1987).
[4] D. Di Carlo, "Inertial microfluidics." Lab Chip **9**, 3038–3046 (2009).
[5] D. J. Pine, J. P. Gollub, J. F. Brady, and A. M. Leshansky, "Chaos and threshold for irreversibility in sheared suspensions." Nat. **438**, 997–1000 (2005).
[6] B. Metzger, P. Pham, and J. E. Butler, "Irreversibility and chaos: Role of lubrication interactions in sheared suspensions," Phys. Rev. E **87**, 052304 (2013).
[7] B. Metzger and J. E. Butler, "Irreversibility and chaos: Role of long-range hydrodynamic interactions in sheared suspensions," Phys. Rev. E **82**, 051406 (2010).
[8] L. Corté, P. M. Chaikin, J. P. Gollub, and D. J. Pine, "Random organization in periodically driven systems," Nat. Phys. **4**, 420–424 (2008).
[9] P. A. Arp and S. G. Mason, "The kinetics of flowing dispersions," J. Colloid Interface Sci. **61**, 44–61 (1977).
[10] F. Gadala-Maria and A. Acrivos, "Shear-induced structure in a concentrated suspension of solid spheres." J. Rheol. **24**, 799–814 (1980).
[11] J. R. Smart and D. T. Leighton Jr., "Measurement of the hydrodynamic surface roughness of noncolloidal spheres," Phys. Fluids A **1**, 52–60 (1989).

[12] F. R. Da Cunha and E. J. Hinch, "Shear-induced dispersion in a dilute suspension of rough spheres," J. Fluid Mech. **309**, 211–223 (1996).

[13] I. E. Zarraga and D. T. Leighton Jr., "Shear-induced diffusivity in a dilute bidisperse suspension of hard spheres," J. Colloid Interface Sci. **243**, 503–514 (2001).

[14] A. Meunier and G. Bossis, "The influence of surface forces on shear-induced tracer diffusion in mono and bidisperse suspensions," Eur. Phys. J. E **25**, 187–199 (2008).

[15] A. L. Graham, S. A. Altobelli, Eiichi Fukushima, L. A. Mondy, and T. S. Stephens, "Note: NMR imaging of shear-induced diffusion and structure in concentrated suspensions undergoing Couette flow," J. Rheol. **35**, 191–201 (1991).

[16] D. M. Husband, L. A. Mondy, E. Ganani, and A. L. Graham, "Direct measurements of shear-induced particle migration in suspensions of bimodal spheres," Rheol. Acta **33**, 185–192 (1994).

[17] M. K. Lyon and L. G. Leal, "An experimental study of the motion of concentrated suspensions in two-dimensional channel flow. Part 2. Bidisperse systems," J. Fluid Mech. **363** (1998), 10.1017/S0022112098008829.

[18] D. Semwogerere and E. R. Weeks, "Shear-induced particle migration in binary colloidal suspensions," Phys. Fluids **20**, 043306 (2008).

[19] C. Gao, B. Xu, and J. F. Gilchrist, "Mixing and segregation of microspheres in microchannel flows of mono- and bidispersed suspensions," Phys. Rev. E **79**, 036311 (2009).

[20] P. Kanehl and H. Stark, "Hydrodynamic segregation in a bidisperse colloidal suspension in microchannel flow: A theoretical study," J. Chem. Phys. **142**, 214901 (2015).

[21] B. Chun, J. S. Park, H. W. Jung, and Y.-Y. Won, "Shear-induced particle migration and segregation in non-brownian bidisperse suspensions under planar poiseuille flow," J. Rheol **63**, 437–453 (2019).

[22] K. Schroen, A. van Dinther, and R. Stockmann, "Particle migration in laminar shear fields: A new basis for large scale separation technology?" Sep. Purif. Technol. **174**, 372–388 (2017).

[23] C. Chang and R. L Powell, "Dynamic Simulation of Bimodal Suspensions of Hydrodynamically Interacting Spherical-Particles," J. Fluid Mech. **253**, 1–25 (1993).

[24] C. Chang and R. L Powell, "Effect of particle size distributions on the rheology of concentrated bimodal suspensions," J. Rheol. **38**, 85 (1994).

[25] C. Chang and R. L. Powell, "The rheology of bimodal hard-sphere dispersions," Phys. Fluids **6**, 1628–1636 (1994).

[26] C. Chang and R. L Powell, "Self-diffusion of bimodal suspensions of hydrodynamically interacting spherical particles in shearing flow," J. Fluid Mech. **281**, 51–80 (1994).

[27] M. Wang and J. F. Brady, "Spectral Ewald Acceleration of Stokesian Dynamics for polydisperse suspensions," J. Comput. Phys. **306**, 443–477 (2016).

[28] M. Wang, M. Heinen, and J. F. Brady, "Short-time diffusion in concentrated bidisperse hard-sphere suspensions," J. Chem. Phys. **142**, 064905 (2015).

[29] M. Wang and J. F. Brady, "Short-time transport properties of bidisperse suspensions and porous media: A Stokesian dynamics study," J. Chem. Phys. **142**, 094901 (2015).

[30] S. Pednekar, J. Chun, and J. Morris, "Bidisperse and polydisperse suspension rheology at large solid fraction," J. Rheol. **62**, 513–526 (2018).

[31] R.E. Hampton, A.A. Mammoli, A.L. Graham, N. Tetlow, and S.A. Altobelli, "Migration of particles undergoing pressure-driven flow in a circular conduit," J. Rheol. **41**, 621–640 (1997).

[32] B. Snook, J. E. Butler, and É. Guazzelli, "Dynamics of shear-induced migration of spherical particles in oscillatory pipe flow," J. Fluid Mech **786**, 128–153 (2016).

[33] H.M. Vollebregt, R.G. Van Der Sman, and R.M. Boom, "Suspension flow modelling in particle migration and microfiltration," Soft Matter **6**, 6052–6064 (2010).

[34] D. Leighton and A. Acrivos, "The shear-induced migration of particles in concentrated suspensions," J. Fluid Mech. **181**, 415–439 (1987).

[35] R. J. Phillips, R. C. Armstrong, R. A. Brown, A. L. Graham, and J. R. Abbott, "A constitutive equation for concentrated suspensions that accounts for shear-induced particle migration," Phys. Fluids **4**, 30–40 (1992).

[36] P. R. Nott and J. F. Brady, "Pressure-driven flow of suspensions: simulation and theory," J. Fluid Mech. **275**, 157 (1994).

[37] J. F. Morris and F. Boulay, "Curvilinear flows of noncolloidal suspensions :," J. Rheol. **43**, 1213–1237 (1999).

[38] A. Shauly, A. Wachs, and A. Nir, "Shear-induced particle migration in a polydisperse concentrated suspension," J. Rheol. **42**, 1329–1348 (1998).

[39] M. M. Reddy and A. Singh, "Shear-induced particle migration and size segregation in bidisperse suspension flowing through symmetric t-shaped channel," Phys. Fluids **31**, 053305 (2019).

[40] R. G. M. van der Sman and H. M. Vollebregt, "Effective temperature for sheared suspensions: A route towards closures for migration in bidisperse suspension," Adv. Colloid Interface Sci. **185-186**, 1–13 (2012).

[41] H. M. Vollebregt, R. G. M. van der Sman, and R. M. Boom, "Model for particle migration in bidisperse suspensions by use of effective temperature," Faraday Discuss. **158**, 89 (2012).

[42] J. T. Norman, B.O. Oguntade, and R.T. Bonnecaze, "Particle-phase distributions of pressure-driven flows of bidisperse suspensions," J. Fluid Mech. **594**, 1–28 (2008).

[43] G. Ovarlez, F. Bertrand, and S. Rodts, "Local determination of the constitutive law of a dense suspension of noncolloidal particles through magnetic resonance imaging," J. Rheol. **50**, 259–292 (2006).

[44] F. Boyer, É. Guazzelli, and O. Pouliquen, "Unifying suspension and granular rheology," Phys. Rev. Lett. **107**, 188301 (2011).

[45] A. Shauly, A. Wachs, and A. Nir, "Shear-induced particle resuspension in settling polydisperse concentrated suspension," Int. J. Multiphas. Flow **26**, 1–15 (2000).

[46] R H Davis and H Gecol, "Hindered settling function with no empirical parameters for polydisperse suspensions," AIChE J. **40**, 570–575 (1994).

[47] P. Gondret and L. Petit, "Dynamic viscosity of macroscopic suspensions of bimodal sized solid spheres," J. Rheol **41**, 1261–1274 (1997).

[48] R. J. Farris, "Prediction of the Viscosity of Multimodal Suspensions from Unimodal Viscosity Data," Trans. Soc. Rheol. **122**, 281–301 (1968).

[49] R. F. Probstein, M. Z. Sengun, and T-C. Tseng, "Bimodal model of concentrated suspension viscosity for distributed particle sizes," J. Rheol. **38**, 811–829 (1994).

[50] R. M. Miller and J. F. Morris, "Normal stress-driven migration and axial development in pressure-driven flow of concentrated suspensions," J. Nonnewton. Fluid Mech. **135**, 149–165 (2006).

[51] K. Yeo and M. R. Maxey, "Simulation of concentrated suspensions using the force-coupling method," J. Comput. Phys. **229**, 2401–2421 (2010).

[52] M. Abbas, E. Climent, O. Simonin, and M. R. Maxey, "Dynamics of bidisperse suspensions under Stokes flows: Linear shear flow and sedimentation," Phys. Fluids **18**, 1–20 (2006).

[53] K. Yeo and M. R. Maxey, "Numerical simulations of concentrated suspensions of monodisperse particles in a Poiseuille flow," J. Fluid Mech. **682**, 491–518 (2011).

[54] S. L. Dance and M. R. Maxey, "Incorporation of lubrication effects into the force-coupling method for particulate two-phase flow," J. Comput. Phys. **189**, 212–238 (2003).

[55] M. R. Maxey and B. K. Patel, "Localized force representations for particles sedimenting in Stokes Flow," Int. J. Multiphas. Flow **27**, 1603–1626 (2001).

[56] S. Lomholt and M. R. Maxey, "Force-coupling method for particulate two-phase flow: Stokes flow," J. Comput. Phys. **184**, 381–405 (2003).

[57] A. Sierou and J. F. Brady, "Rheology and microstructure in concentrated noncolloidal suspensions," J. Rheol. **46**, 1031–1056 (2002).

[58] N.-Q. Nguyen and A. J. C. Ladd, "Lubrication corrections for lattice-Boltzmann simulations of particle suspensions," Phys. Rev. E **66**, 046708 (2002).

[59] A. A. Howard, "Source code for generating lubrication resistance functions," *Data Publ. Brown Digit. Repos. Brown Univ. Libr.*, (2018), doi:10.7301/Z05B00ZM.

[60] D. J. Jeffrey and Y. Onishi, "Calculation of the resistance and mobility functions for two unequal rigid spheres in low-Reynolds-number flow," J. Fluid Mech. **139**, 261 (1984).

[61] D. J. Jeffrey, "The calculation of the low Reynolds number resistance functions for two unequal spheres," Phys. Fluids A **4**, 16–29 (1992).

[62] S. Kim and S. J. Karrila, *Microhydrodynamics : Principles and Selected Applications* (Dover Publications, Inc., 1991) p. 503.

[63] K. Ichiki, "Errata on the papers for two-body exact solutions in Stokes flows," http://ryuon.sourceforge.net/twobody/errata.html (2008).

[64] A. K. Townsend, "Generating, from scratch, the near-field asymptotic forms of scalar resistance functions for two unequal rigid spheres in low-Reynolds-number flow," (2018), arXiv:1802.08226.

[65] A. J. C. Ladd, "Hydrodynamic transport coefficients of random dispersions of hard spheres," J. Chem. Phys. **93**, 3484–3494 (1990).

[66] G. K. Batchelor, "The stress system in a suspension of force-free particles," J. Fluid Mech. **41**, 545 (1970).

[67] R. Glowinski, T.W. Pan, T.I. Hesla, D.D. Joseph, and J. Periaux, "A fictitious domain approach to the direct numerical simulation of incompressible viscous flow past moving rigid bodies: application to particulate flow," J. Comput. Phys. **169**, 363–426 (2001).

[68] Z. Yu and X. Shao, "A direct-forcing fictitious domain method for particulate flows," J. Comput. Phys. **227**, 292–314 (2007).

[69] S. Gallier, E. Lemaire, L. Lobry, and F. Peters, "A fictitious domain approach for the simulation of dense suspensions," J. Comput. Phys. **256**, 367–387 (2014).

[70] J.F. Brady and G. Bossis, "The rheology of concentrated suspensions of spheres in simple shear flow by numerical simulation," J. Fluid Mech. **155**, 105–129 (1985).

[71] G. K. Batchelor and J. T. Green, "The hydrodynamic interaction of two small freely-moving spheres in a linear flow field," J. Fluid Mech. **56**, 375 (1972).

[72] Raphael Pesche, *Etude par simulation numerique de la segregation de particules dans une suspension bidisperse*, Ph.D. thesis (1998).

[73] D. A. Drew, "Mathematical Modeling of Two-Phase Flow," Annu. Rev. Fluid Mech. **15**, 261–291 (1983).

[74] K. Yeo and M. R. Maxey, "Dynamics of concentrated suspensions of non-colloidal particles in Couette flow," J. Fluid Mech. **649**, 205 (2010).

[75] C. Gamonpilas, J. F. Morris, and M. M. Denn, "Shear and normal stress measurements in non-Brownian monodisperse and bidisperse suspensions," J. Rheol. **60**, 289–296 (2016).

[76] C. Gamonpilas, J. F. Morris, and M. M. Denn, "Erratum: "Shear and normal stress measurements in non-Brownian monodisperse and bidisperse suspensions"," J. Rheol. **62**, 665–667 (2018).

[77] I. E. Zarraga, D. A. Hill, and D. T. Leighton Jr., "The characterization of the total stress of concentrated suspensions of noncolloidal spheres in Newtonian fluids," J. Rheol. **44**, 671 (2000).
[78] S. Gallier, E. Lemaire, F. Peters, and L. Lobry, "Rheology of sheared suspensions of rough frictional particles," J. Fluid Mech. **757**, 514–549 (2014).
[79] S. Gallier, E. Lemaire, L. Lobry, and F. Peters, "Effect of confinement in wall-bounded non-colloidal suspensions," J. Fluid Mech. **799**, 100–127 (2016).
[80] F. R. Cui, A. A. Howard, M. R. Maxey, and A. Tripathi, "Dispersion of a suspension plug in oscillatory pressure-driven flow," Phys. Rev. Fluids **2**, 094303 (2017).